PERGAMON

International Journal of Heat and Mass Transfer 45 (2002) 4543–4559

International Journal of HEAT and MASS TRANSFER

www.elsevier.com/locate/ijhmt

Role of length scales on microwave thawing dynamics in 2D cylinders

Tanmay Basak *, K.G. Ayappa

Department of Chemical Engineering, Indian Institute of Science, Bangalore 560012, India

Received 31 March 2001; received in revised form 30 April 2002

Abstract

Microwave (MW) thawing of 2D frozen cylinders exposed to uniform plane waves from one face, is modeled using the effective heat capacity formulation with the MW power obtained from the electric field equations. Computations are illustrated for tylose (23% methyl cellulose gel) which melts over a range of temperatures giving rise to a mushy zone. Within the mushy region the dielectric properties are functions of the liquid volume fraction. The resulting coupled, time dependent non-linear equations are solved using the Galerkin finite element method with a fixed mesh. Our method efficiently captures the multiple connected thawed domains that arise due to the penetration of MWs in the sample. For a cylinder of diameter D, the two length scales that control the thawing dynamics are D/D_p and D/λ_m, where D_p and λ_m are the penetration depth and wavelength of radiation in the sample respectively. For $D/D_p, D/\lambda_m \ll 1$ power absorption is uniform and thawing occurs almost simultaneously across the sample (Regime I). For $D/D_p \gg 1$ thawing is seen to occur from the incident face, since the power decays exponentially into the sample (Regime III). At intermediate values, $0.2 < D/D_p, D/\lambda_m < 2.0$ (Regime II) thawing occurs from the unexposed face at smaller diameters, from both faces at intermediate diameters and from the exposed and central regions at larger diameters. Average power absorption during thawing indicates a monotonic rise in Regime I and a monotonic decrease in Regime III. Local maxima in the average power observed for samples in Regime II are due to internal resonances within the sample. Thawing time increases monotonically with sample diameter and temperature gradients in the sample generally increase from Regime I to Regime III.

© 2002 Elsevier Science Ltd. All rights reserved.

Keywords: Microwave; Thawing; Length scales; 2D finite elements

1. Introduction

Various food industries preserve food at the frozen state prior to thawing. Thawing can be carried out by conventional surface heating or with microwaves (MWs) which provides a volumetrically distributed heat source. Conventional thawing, in addition to requiring long processing times and large space requirements, increases the risk of chemical and biological deterioration of the food product [1,2]. In contrast, MW thawing, if effectively used can result in shorter processing times. In addition to finding widespread use in domestic MW ovens, MWs can potentially be exploited for rapid thawing of frozen biological organs prior to transplants.

One of the main challenges associated with MW thawing lies in achieving uniform temperatures in the final thawed product. Non-uniformity in heating arises due to the uneven power distributions and the increasing power absorption in liquid regions. Since most biological systems are multicomponent in nature, the phase change occurs over a finite temperature range. Within this temperature range the equilibrium phase made up of coexisting solid and liquid is commonly referred to as the 'mushy' region. In addition to the formation of the

* Corresponding author. Address: Department of Chemistry, Air Quality Modeling Center, University of Houston, 136 Fleming Building, Houston, TX 77204-5003, USA. Tel.: +1-713-743-0758; fax: +1-713-743-2709.

E-mail addresses: tbasak@bayou.uh.edu (T. Basak), ayappa@chemeng.iisc.ernet.in (K.G. Ayappa).

0017-9310/02/$ - see front matter © 2002 Elsevier Science Ltd. All rights reserved.
PII: S0017-9310(02)00171-0

Nomenclature

Bi	Biot number
c	velocity of light, $m\,s^{-1}$
C_{eff}	effective heat capacity, $J\,m^{-3}\,K^{-1}$
C	specific heat capacity, $J\,kg^{-1}\,K^{-1}$
D_p	penetration depth, m
E_z	electric field intensity, $V\,m^{-1}$
E_0	incident electric field intensity, $V\,m^{-1}$
f	frequency, Hz
h	heat transfer coefficient, $W\,m^{-2}\,K^{-1}$
H	specific enthalpy, $J\,m^{-3}$
I_0	flux of incident radiation, $W\,m^{-2}$
k	thermal conductivity, $W\,m^{-1}\,K^{-1}$
k	propagation constant
k_0	reference thermal conductivity, $W\ m^{-1}\,K^{-1}$
k_{eff}	effective thermal conductivity, $W\,m^{-1}\,K^{-1}$
p	microwave (MW) source term, $W\,m^{-3}$
P	dimensionless MW source term
R	radius of cylinder, m
s_d	shape factor
t	time, s
T	temperature, K
T_i	initial melting point, K
T_m	melting point, K
T_f	final melting point, K
T_∞	ambient temperature, K
T_0	initial temperature, K
v_z	dimensionless real field component
w_z	dimensionless imaginary field component

Greek symbols

α	wave number, m^{-1}
α_0	reference thermal diffusivity, $m^2\,s^{-1}$
β	attenuation constant, m^{-1}
γ	dimensionless propagation constant
ϵ_0	free space permittivity, $Farad\,m^{-1}$
θ	dimensionless temperature
κ'	relative dielectric constant
κ''	relative dielectric loss
κ^*	complex relative dielectric constant
λ	latent heat, $J\,kg^{-1}$
λ_0	wavelength in the free space, m
λ_m	wavelength in the medium, m
ρ	density, $kg\,m^{-3}$
τ	dimensionless time
ψ	basis functions
ϕ_l	liquid volume fraction
ω	angular frequency, $Rad\,s^{-1}$

Subscripts

c	continuous phase
d	dispersed phase
f	frozen phase
l	liquid phase

Superscripts

n	newton iterate index
t	time index

mushy region, models for the dynamics of MW thawing are further complicated due to the penetration of MWs which results in multiply connected liquid domains within the sample. A successful model for MW thawing must be able to capture these partially thawed regions.

Models describing thawing of materials with a unique melting point are known as *temperature methods* [3]. The temperature methods are in reality valid for pure substances and the numerical algorithm should be able to track the phase change interface. Although tractable in 1D this approach can get quite cumbersome, if not impossible for MW thawing in higher dimensions where the phase change front may appear in any region due to the penetration of MWs. A number of earlier studies on MW thawing, based on the temperature method were restricted to 1D systems [4–6].

Models for food substances which melt over a range of temperatures are known as *enthalpy or effective heat capacity method* [7–9]. In the effective heat capacity method, a single energy balance equation is used for the entire domain, which may consist of frozen, mush and liquid regions. The key advantage of the method is the absence of a front tracking algorithm and the method, as we have demonstrated in 1D [10] can easily handle multiple thawed regions which frequently arise during MW thawing. In addition this method can be extended for pure substances with an introduction of a superficial mushy region at the phase change temperature [11]. A few studies on MW thawing, based on the effective heat capacity method [12,13] have been carried out with a Lambert's law formulation of the MW power. Zeng and Faghri [13] using a 2D model studied the thawing of tylose (23% methyl cellulose gel) and found that the temperatures predicted at the end of thawing were lower than the experimentally observed values.

In a previous work we illustrated the efficacy of the effective heat capacity formulation for modeling phase change in 1D slabs with MWs [10]. Using the finite element method, temperatures and power distributions were obtained by solving the effective heat capacity based energy balance equation with Maxwell's equations for the propagation of MWs [14]. The computations were carried out for tylose, whose dielectric and thermal properties are similar to those of frozen meats and is used extensively in previous MW thawing models and experiments. Our 1D studies reveal that thawing is ini-

tiated from the center or from the outer surface depending on the thickness of the slab and that the effective heat capacity method captures these situations with little computational effort. Resonances, during which MW power absorption is high, have been found when a sample is incident with MWs at both faces causing the 2 cm slab to thaw quicker than 1 cm slabs.

Encouraged by our results in 1D, we carried out some preliminary studies of MW thawing in 2D cylinders [15]. Here we carry out a detailed analysis of MW thawing of tylose using the effective heat capacity method for 2D cylinders exposed to uniform plane waves at 2450 MHz. The energy balance equation, nonlinearly coupled with the Maxwell's equations is solved using the Galerkin finite element method to obtain the absorbed MW power, temperature and liquid volume fraction profiles for various cylinder diameters. We illustrate a number of different thawing scenarios that arise when the diameter of the sample is varied and generalize the trends based on the ratios of the sample diameter to the penetration depth and wavelength of radiation in the medium. Average power values, temperatures and total thawing times are reported as well.

2. Theory

2.1. Effective heat capacity formulation

Consider a partially thawed sample consisting of a solid, liquid and a mushy zone as shown in Fig. 1. In the effective heat capacity method the temperature at any point in the sample is obtained by solving the single energy balance equation for the entire domain;

$$C_{\text{eff}}\frac{\partial T}{\partial t} = \nabla \cdot k_{\text{eff}}\nabla T + p(T), \tag{1}$$

The effective heat capacity,

$$C_{\text{eff}} = \mathrm{d}H/\mathrm{d}T, \tag{2}$$

and the temperature dependent enthalpy,

$$H(T) = (1-\phi_{\text{l}})\int_{T_0}^{T}\rho C_{\text{s}}(\alpha)\,\mathrm{d}\alpha + \phi_{\text{l}}\left[\int_{T_0}^{T_{\text{i}}}\rho C_{\text{s}}(\alpha)\,\mathrm{d}\alpha + \rho\lambda + \int_{T_{\text{i}}}^{T}\rho C_{\text{l}}(\alpha)\,\mathrm{d}\alpha\right], \tag{3}$$

where C_{l} and C_{s} are the heat capacities of the liquid and solid phases respectively, T_0 is a reference temperature, T_{i} the initial melting point and ϕ_{l}, the liquid volume fraction is a function of the temperature at a given point in the sample. The functional form of ϕ_{l} vs T is an equilibrium relationship which can be obtained from the phase diagram of the material being thawed or from calorimetric measurements. In Eq. (1) the effective thermal conductivity, $k_{\text{eff}} = \phi_{\text{l}}k_{\text{l}} + (1-\phi_{\text{l}})k_{\text{s}}$, where k_{l} and k_{s} are the thermal conductivities of the liquid and solid phases respectively and $p(T)$ the absorbed MW power is proportional to the electric field intensity in the sample and the frequency dependent dielectric loss. The density difference between the solid and liquid phase is assumed to be small, and ρ in Eq. (3) represents a mean density between the two phases. We have neglected buoyancy induced convection in the liquid regime based on our recent analysis [16]. In addition, neglecting buoyancy effects is a good approximation for thawing of highly viscous food substances such as tylose. For most food substances, C_{eff} is a continuous function of temperature. However, discontinuities can occur in C_{eff} depending on the functional form of ϕ_{l} vs T (e.g. NaCl, [11]).

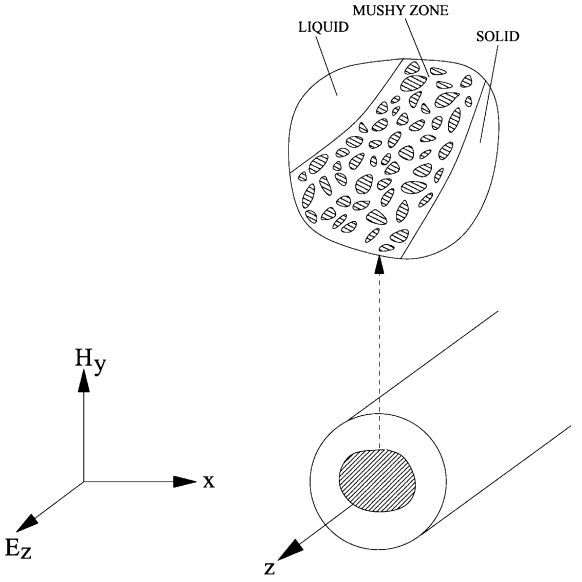

Fig. 1. Schematic illustrating the liquid, solid and mushy region in a partly thawed sample exposed to a plane electromagnetic wave. The incident electric field is oriented along the axis (z-axis) of the cylinder.

We consider the MW thawing in a cylinder of radius R exposed to uniform plane waves as shown in Fig. 1. Initially the sample is completely frozen at a uniform temperature T_0. The thermal properties in the cylinder is assumed to be isotropic and the surrounding medium is at the ambient temperature, T_∞, during the entire thawing period. At the sample boundaries heat is lost by convection. Using the following dimensionless variables,

$$\nabla^* = R\nabla, \quad \theta = \frac{T-T_\infty}{T_0}, \quad B_i = \frac{hR}{k} \quad \text{and} \quad \tau = \frac{\alpha_0 t}{R^2}. \tag{4}$$

The dimensionless form of Eq. (3) is

$$\overline{C}_{\text{eff}}\frac{\partial\theta}{\partial\tau} = \nabla^* \cdot (\bar{k}_{\text{eff}}\nabla^*\theta) + P(\theta), \tag{5}$$

where $P = (pR^2)/(k_0T_0)$, $\overline{C}_{\text{eff}} = C_{\text{eff}}/(\rho_0 C_{p,0})$ and $\bar{k}_{\text{eff}} = k_{\text{eff}}/k_0$. Here ρ_0, $C_{p,0}$, k_0 and α_0 are the reference density, heat capacity, thermal conductivity and thermal diffusivity, respectively. The initial condition is

$$\theta(\tau = 0) = \frac{T_0 - T_\infty}{T_0} \quad \text{for} -1 \leqslant x, y \leqslant 1, \tag{6}$$

and the boundary condition is

$$-\mathbf{n} \cdot \bar{k}_{\text{eff}} \nabla^* \theta = Bi\theta. \tag{7}$$

The temperature dependent MW power term in Eq. (5) is obtained by solving the equations for the electric field simultaneously with Eq. (5).

2.2. Electric field equations for a cylinder

The incident MW is a uniform plane wave, with the electric and magnetic components varying in intensity only in the direction of wave propagation (x-axis). The orientation of the incident wave shown in Fig. 1 is known as the transverse magnetic or TM^z polarization, since the magnetic field is perpendicular to the cylinder axis. If the electric field is oriented perpendicular to the axis, the polarization is TE^z or transverse electric. Previous studies [17] have shown that the TE^z polarization couples weakly with the sample, and we only consider the TM^z polarization in this study. In this situation Maxwell's equations reduce to a single equation for the electric field, E_z, [18],

$$\nabla^2 E_z + \kappa^2(\phi_l) E_z = 0, \tag{8}$$

where ϕ_l is the liquid volume fraction and

$$k = \frac{\omega}{c}\sqrt{\kappa'(\phi_l) + \mathrm{i}\kappa''(\phi_l)} \tag{9}$$

is the spatially varying propagation constant dependent on $\kappa'(\phi_l)$, the relative dielectric constant and $\kappa''(\phi_l)$, the relative dielectric loss. The dielectric constant measures the ability to store electric energy and the dielectric loss measures the ability to convert electric energy into heat. Here $\omega = 2\pi f$, where f is the frequency of the electromagnetic wave and c is the velocity of light. We assume that the dielectric properties are temperature dependent only due to their dependence on ϕ_l. Hence in regions of pure liquid and solid the dielectric properties are assumed to be independent of temperature. Previous studies on the influence of temperature dependent dielectric properties indicate that this is a good assumption at 2450 MHz [19]. The penetration depth D_p and wavelength of radiation in the medium λ_m are related to κ' and κ'' in the following manner;

$$D_p = \frac{c}{\sqrt{2}\pi f\left[\kappa'\left(\sqrt{1 + \left(\frac{\kappa''}{\kappa'}\right)^2} - 1\right)\right]^{1/2}} \tag{10}$$

and

$$\lambda_m = \frac{c\sqrt{2}}{f\left[\kappa'\left(\sqrt{1 + \left(\frac{\kappa''}{\kappa'}\right)^2} + 1\right)\right]^{1/2}}. \tag{11}$$

Using the expressions for D_p and λ_m, the propagation constant in Eq. (8) can be written as

$$k = (2\pi/\lambda_m) + \mathrm{i}(1/D_p). \tag{12}$$

The above form of the propagation constant indicates that λ_m and D_p are the two length scales that determine the electric field distribution in the sample. D_p is defined as the distance at which the electric field decays to $1/e$ of its incident value. Although strictly defined for semi-infinite samples, it nevertheless provides a useful measure for the penetration of MWs. For most biological materials, the typical range for λ_m and D_p are 1–10 cm.

The expression for the relative complex dielectric constant $\kappa^* = \kappa' + \mathrm{i}\kappa''$ in the mushy zone, based on Fricke's [20] complex conductivity model is

$$\kappa^* = \frac{\kappa_c^*[\kappa_d^*(1 + s_d V_d) + \kappa_c^*(1 - V_d)s_d]}{[\kappa_c^*(s_d + V_d) + \kappa_d^*(1 - V_d)]}, \tag{13}$$

where κ_c^* and κ_d^* are the relative complex dielectric properties of the continuous and dispersed phases respectively, $s_d = 2$ for spherical dispersions and $s_d = 1$ for cylindrical dispersions. V_d the volume fraction of the dispersed phase, is $1 - \phi_l$, when the solid is the dispersed phase (liquid continuous) and $V_d = \phi_l$, when liquid is the dispersed phase (solid continuous). The effective dielectric constants in the mushy zone depend on whether the solid or liquid forms the continuous phase. Though previous studies [4,5] are carried out by assuming that the solid forms the continuous phase, a recent model for MW thawing by Basak and Ayappa [10] is based on the knowledge that melting is initiated at the grain boundaries of the solid phase and the microstructure of the mushy region is typically characterized by a solid dispersed in a continuous liquid phase. A comparison between the liquid continuous and solid continuous models shows that thawing dynamics can be quite different due to the increased penetration depth for the solid continuous model [10].

The power absorbed per unit volume is

$$p = \tfrac{1}{2}\omega\epsilon_0\kappa'' E_z E_z^*, \tag{14}$$

where ϵ_0 is the free space permittivity and E_z^* is the complex conjugate of E_z. For a given flux of incident radiation, I_0, in free space the incident electric field intensity E_0, is given by,

$$E_0 = \sqrt{\frac{2I_0}{c\epsilon_0}}. \tag{15}$$

It is assumed in the model that the liquid and solid phases are always separated by a mushy region (Fig. 1) which is found to be true for all the cases simulated here. This coupled with the continuity of the ϕ_l vs T relationship always ensures that the dielectric properties are continuous across the slab. Hence, interface conditions between solid and mush or liquid and mush are not required while solving the electric field equation.

Using the dimensionless variables,

$$u_z = \frac{E_z}{E_0} \quad \text{and} \quad \nabla^* = R\nabla,$$

Eq. (8) reduces to

$$\nabla^{*2} u_z + \gamma^2(\phi_l) u_z = 0, \tag{16}$$

where u_z is the electric field intensity and $\gamma(\phi_l) = ((R\omega)/c)\sqrt{\kappa'(\phi_l) + i\kappa''(\phi_l)}$ is the propagation constant. Note that if the propagation constant is expressed in terms of D_p and λ_m (Eq. 12) then the expression for γ in terms of the two length scales D/D_p and D/λ_m where D is the diameter of the cylinder is,

$$\gamma = \frac{D\pi}{\lambda_m} + i\frac{D}{2D_p}. \tag{17}$$

Although we use the expression for γ in terms of the fundamental properties κ' and κ'' for our computations, the two length scales D/D_p and D/λ_m will be useful while interpreting our results. Substituting the complex field variable $u_z = v_z + iw_z$ into Eq. (16) and equating the real and imaginary components

$$\nabla^{*2} v_z + \chi_1(\phi_l) v_z - \chi_2(\phi_l) w_z = 0 \tag{18}$$

and

$$\nabla^{*2} w_z + \chi_2(\phi_l) v_z + \chi_1(\phi_l) w_z = 0, \tag{19}$$

where $\chi_1(\phi_l) = ((R^2\omega^2)/c^2)\kappa'(\phi_l)$ and $\chi_2(\phi_l) = ((R^2\omega^2)/c^2)\kappa''(\phi_l)$.

For uniform plane waves incident on a sample some of the radiation is scattered and the rest absorbed. The radiation boundary conditions [17] for the electric field are used at the outer surface of the cylinder. The boundary conditions for v_z and w_z are,

$$\begin{aligned}\mathbf{n}\cdot\nabla^* v_z = {} & \sum_{n=0}^{\infty} \mathrm{Re}(C_n)\cos n\phi + \sum_{n=0}^{\infty} \mathrm{Re}(D_n) \\ & \times \int_0^{2\pi} v_z(1,\phi')\cos n(\phi-\phi')\,\mathrm{d}\phi' \\ & - \sum_{n=0}^{\infty} \mathrm{Im}(D_n) \int_0^{2\pi} w_z(1,\phi')\cos n(\phi-\phi')\,\mathrm{d}\phi'\end{aligned} \tag{20}$$

and

$$\begin{aligned}\mathbf{n}\cdot\nabla^* w_z = {} & \sum_{n=0}^{\infty} \mathrm{Im}(C_n)\cos n\phi + \sum_{n=0}^{\infty} \mathrm{Im}(D_n) \\ & \times \int_0^{2\pi} v_z(1,\phi')\cos n(\phi-\phi')\,\mathrm{d}\phi' \\ & + \sum_{n=0}^{\infty} \mathrm{Re}(D_n) \int_0^{2\pi} w_z(1,\phi')\cos n(\phi-\phi')\,\mathrm{d}\phi',\end{aligned} \tag{21}$$

where the coefficients

$$C_n = \epsilon_n i^n \omega^* \left[J_n'(\omega^*) - J_n(\omega^*) \frac{H_n^{(1)'}(\omega^*)}{H_n^{(1)}(\omega^*)} \right] \tag{22}$$

and

$$D_n = \frac{\omega^* \delta_n H_n^{(1)'}(\omega^*)}{\pi H_n^{(1)}(\omega^*)} \tag{23}$$

and

$$\epsilon_n = \begin{cases} 1, & n = 0; \\ 2, & \text{otherwise}, \end{cases} \quad \text{and} \quad \delta_n = \begin{cases} 1/2, & n = 0; \\ 1, & \text{otherwise}. \end{cases} \tag{24}$$

In Eqs. (22) and (23) $\omega^* = \omega R/c$, J_n and $H_n^{(1)}$ are the Bessel and Hankel functions of the first kind respectively. The prime indicates the first derivatives [21]. The expression for the MW power term in Eq. (14) is

$$P(\phi_l(\theta)) = \frac{R^2 \omega \epsilon_0 \kappa''(\phi_l) E_0^2}{2k_0 T_0} (v_z^2 + w_z^2). \tag{25}$$

It is instructive to rewrite the expression for the dimensionless MW power in terms of D/λ_m and D/D_p. Substituting the expression for κ'' obtained by equating the real and imaginary parts of Eq. (9) with Eq. (12) and replacing E_0 with I_0 from Eq. (15) and Eq. (25) reduces to

$$P = \left(\frac{D}{\lambda_m}\right)\left(\frac{D}{D_p}\right) G(v_z^2 + w_z^2), \tag{26}$$

where $G = \lambda_0 I_0/(2k_0 T_0)$. For a fixed incident frequency, f, of the MW field and for a given material, the free space wavelength λ_0, and the wavelength and penetration depth in the medium λ_m and D_p respectively are fixed. For fixed thermal properties the only variables that can be varied independently are the sample diameter D and the incident field intensity I_0. The form of Eq. (26) illustrates the manner in which various electric field parameters enter the energy balance equation.

2.3. Solution procedure

The energy balance equation, Eq. (5) and the electric field equations, Eqs. (18) and (19), are solved using the Galerkin finite element method. The symmetry of the MW radiation with respect to $y = 0$ as shown in Fig. 2 results in a temperature distribution which is also

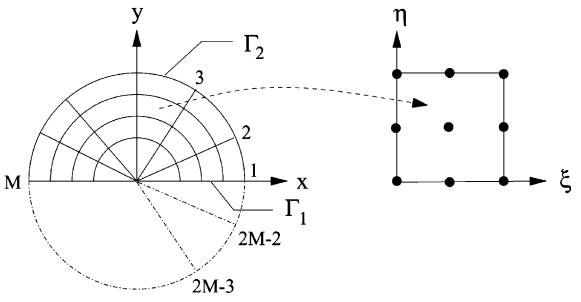

Fig. 2. Illustration of the mesh used in the finite element study for the cylindrical half domain. Symmetry conditions both for the electric field components and temperature are imposed on Γ_1. Mapping from x–y to ξ–η for a representative element is shown.

symmetric with respect to $y = 0$. Hence, we solve the equations only in the upper-half of the cylinder as shown in Fig. 2. Expanding the real (v_z) and imaginary components (w_z) of the electric field, and the temperature (θ) in a basis set $\{\psi\}$,

$$v_z \approx \sum_{k=1}^{N} v_{z,k}\psi_k(x,y),$$
$$w_z \approx \sum_{k=1}^{N} w_{z,k}\psi_k(x,y) \quad \text{and} \quad \theta \approx \sum_{k=1}^{N} \theta_k\psi_k(x,y), \tag{27}$$

for $-1 \leqslant x, y \leqslant 1$, the Galerkin finite element method yields the following non-linear residual equations for Eqs. (18), (19) and (5) respectively.

$$R_i^{(1)} = \sum_{k=1}^{N} v_{z,k}^{t+1} \int_\Omega \left[\frac{\partial\psi_i}{\partial x}\frac{\partial\psi_k}{\partial x} + \frac{\partial\psi_i}{\partial y}\frac{\partial\psi_k}{\partial y}\right] \mathrm{d}x\,\mathrm{d}y + \sum_{k=1}^{N} w_{z,k}^{t+1} \int_\Omega \chi_2\left(\phi_1^{t+1}\right)\psi_i\psi_k \,\mathrm{d}x\,\mathrm{d}y - \sum_{k=1}^{N} v_{z,k}^{t+1} \times \int_\Omega \chi_1\left(\phi_1^{t+1}\right)\psi_i\psi_k \,\mathrm{d}x\,\mathrm{d}y - \int_{\Gamma_2} \psi_i \mathbf{n}\cdot\nabla^* v_z^{t+1}\,\mathrm{d}\Gamma, \tag{28}$$

$$R_i^{(2)} = \sum_{k=1}^{N} w_{z,k}^{t+1} \int_\Omega \left[\frac{\partial\psi_i}{\partial x}\frac{\partial\psi_k}{\partial x} + \frac{\partial\psi_i}{\partial y}\frac{\partial\psi_k}{\partial y}\right] \mathrm{d}x\,\mathrm{d}y - \sum_{k=1}^{N} v_{z,k}^{t+1} \int_\Omega \chi_2\left(\phi_1^{t+1}\right)\psi_i\psi_k \,\mathrm{d}x\,\mathrm{d}y - \sum_{k=1}^{N} w_{z,k}^{t+1} \times \int_\Omega \chi_1\left(\phi_1^{t+1}\right)\psi_i\psi_k \,\mathrm{d}x\,\mathrm{d}y - \int_{\Gamma_2} \psi_i \mathbf{n}\cdot\nabla^* w_z^{t+1}\,\mathrm{d}\Gamma \tag{29}$$

$$R_i^{(3)} = \sum_{k=1}^{N} \int_\Omega \left[\overline{C}_{\mathrm{eff}}\left(\phi_1^{t+1}, \theta^{t+1}\right)\right]\left\{\frac{\theta_k^{t+1} - \theta_k^t}{\Delta\tau}\right\}\psi_i\psi_k \,\mathrm{d}x\,\mathrm{d}y + \frac{1}{2}\left[F(\theta^{t+1}, v_z^{t+1}, w_z^{t+1}, \phi_1^{t+1}) + F(\theta^t, v_z^t, w_z^t, \phi_1^t)\right] \tag{30}$$

where

$$F(\theta^t, v_z^t, w_z^t, \phi_1^t) = \sum_{k=1}^{N} \theta_k^t \int_\Omega \bar{k}_{\mathrm{eff}}(\phi_1^t)\left[\frac{\partial\psi_i}{\partial x}\frac{\partial\psi_k}{\partial x} + \frac{\partial\psi_i}{\partial y}\frac{\partial\psi_k}{\partial y}\right]\mathrm{d}x\,\mathrm{d}y + \int_{\Gamma_2} \psi_i Bi\theta^t\,\mathrm{d}\Gamma - \frac{R^2\omega\epsilon_0 E_0^2}{2k_0 T_0} \times \int_\Omega \kappa''(\phi_1^t)\left\{\left(\sum_k v_{z,k}^t\psi_k\right)^2 + \left(\sum_k w_{z,k}^t\psi_k\right)^2\right\}\psi_i\,\mathrm{d}x\,\mathrm{d}y \tag{31}$$

and $i = 1 \ldots N$ and t is the time index. The gradients of the electric field in the surface integrals due to RBC of Eqs. (28) and (29) are evaluated using Eqs. (20) and (21). Evaluation of RBC for a half domain (Fig. 2) is discussed later. The unconditionally stable Crank–Nicholson algorithm, is used to discretize the time domain in Eq. (30) and biquadratic basis functions with three point Gaussian quadrature is used to evaluate the integrals in the residual equations. The non-linear residual equations (Eqs. (28)–(30)) are solved using a Newton–Raphson procedure, to determine the coefficients of the expansions in Eq. (27) at each time step. At each time step, the linear ($3N \times 3N$) system solved is

$$\mathbf{J}\left(\mathbf{u}^{n,t+1}\right)\left[\mathbf{u}^{n,t+1} - \mathbf{u}^{n+1,t+1}\right] = \mathbf{R}\left(\mathbf{u}^{n,t+1}\right), \tag{32}$$

where n is the Newton iterate index and t the time index. The elements of the Jacobian matrix, $\mathbf{J}(\mathbf{u}^{n,t+1})$ contains the derivatives of the residual equations with respect to the temperature (θ_j's) and electric field unknowns (v_j's and w_j's) and $\mathbf{R}(\mathbf{u}^{n,t+1})$ is the vector of residuals.

2.4. Domain discretizations and integrations

Finite element meshes for the computational domain are shown in Fig. 2. Mesh numbering from the center outward was used in both the cases. The convective boundary conditions for the heat transfer, Eq. (7) and the RBC, Eqs. (20) and (21) are imposed on Γ_2 whereas no flux heat transfer boundary conditions and zero RBC are imposed on Γ_1. We have used nine node biquadratic elements with each element mapped using isoparametric mapping [22] from x–y to a unit square ξ–η domain as shown in Fig. 2. Correspondingly, the domain integrals in the residual equations are evaluated using nine node biquadratic basis functions in ξ–η domain using:

$$x = \sum_{i=1}^{9} x_i\psi_i(\xi,\eta) \quad \text{and} \quad y = \sum_{i=1}^{9} y_i\psi_i(\xi,\eta), \tag{33}$$

where $\psi_i(\xi,\eta)$ are the local biquadratic basis functions on the ξ–η domain. At the center of the cylinder col-

lapsed elements are used where three nodes share the coordinates at the origin.

2.5. RBC for the half domain

In this section, we evaluate the boundary integrals for the RBC in Eqs. (28) and (29) for the half domain, Γ_2 as illustrated in Fig. 2. The RBC derived here is similar to that developed in Ref. [16], and is included here for completion. With the finite element expansions in Eq. (27) and RBC's from Eqs. (20) and (21), the boundary integrals for M nodes on Γ_2 are,

$$\begin{aligned}
&\int_{\Gamma_2} \psi_i \mathbf{n}\cdot\nabla^* v_z \,\mathrm{d}\Gamma \\
&= \sum_n^{\infty} \mathrm{Re}(C_n)\xi^h_{in} + \sum_{j=1}^{M} v_j \\
&\quad\times \sum_{n=0}^{\infty} \mathrm{Re}(D_n)\Big[\xi^h_{in}\Big(\xi^f_{j,n} + \beta_{1j}\beta_{Mj}\xi^f_{2M-j,n}\Big) \\
&\qquad + \eta^h_{in}\Big(\eta^f_{j,n} + \beta_{1j}\beta_{Mj}\eta^f_{2M-j,n}\Big)\Big] - \sum_{j=1}^{M} w_j \\
&\quad\times \sum_{n=0}^{\infty} \mathrm{Im}(D_n)\Big[\xi^h_{in}\Big(\xi^f_{j,n} + \beta_{1j}\beta_{Mj}\xi^f_{2M-j,n}\Big) \\
&\qquad + \eta^h_{in}\Big(\eta^f_{j,n} + \beta_{1j}\beta_{Mj}\eta^f_{2M-j,n}\Big)\Big], \qquad (34)
\end{aligned}$$

and

$$\begin{aligned}
&\int_{\Gamma_2} \psi_i \mathbf{n}\cdot\nabla^* w_z \,\mathrm{d}\Gamma \\
&= \sum_n^{\infty} \mathrm{Im}(C_n)\xi^h_{in} + \sum_{j=1}^{M} v_j \\
&\quad\times \sum_{n=0}^{\infty} \mathrm{Im}(D_n)\Big[\xi^h_{in}\Big(\xi^f_{j,n} + \beta_{1j}\beta_{Mj}\xi^f_{2M-j,n}\Big) \\
&\qquad + \eta^h_{in}\Big(\eta^f_{j,n} + \beta_{1j}\beta_{Mj}\eta^f_{2M-j,n}\Big)\Big] + \sum_{j=1}^{M} w_j \\
&\quad\times \sum_{n=0}^{\infty} \mathrm{Re}(D_n)\Big[\xi^h_{in}\Big(\xi^f_{j,n} + \beta_{1j}\beta_{Mj}\xi^f_{2M-j,n}\Big) \\
&\qquad + \eta^h_{in}\Big(\eta^f_{j,n} + \beta_{1j}\beta_{Mj}\eta^f_{2M-j,n}\Big)\Big], \qquad (35)
\end{aligned}$$

where

$$\left.\begin{aligned}
\xi^h_{ln} &= \int_0^{\pi} \cos n\alpha\,\psi_1 \,\mathrm{d}\alpha, \quad \xi^f_{ln} = \int_0^{2\pi} \cos n\alpha\,\psi_1 \,\mathrm{d}\alpha \\
\eta^h_{ln} &= \int_0^{\pi} \sin n\alpha\,\psi_1 \,\mathrm{d}\alpha, \quad \eta^f_{ln} = \int_0^{2\pi} \sin n\alpha\,\psi_1 \,\mathrm{d}\alpha
\end{aligned}\right\} \quad l = i, j. \qquad (36)$$

and $\beta_{ij} = 1 - \delta_{ij}$, where δ_{ij} is the Kronecker delta symbol, with the property

$$\delta_{ij} = \begin{cases} 0, & i \neq j, \\ 1, & i = j. \end{cases} \qquad (37)$$

The summations over the index, n, refer to the coefficients involving Bessel functions. Typically $n = 15$–20. Note that the RBC involves integrals for the full domain as well as for the half domain. The full domain, $(0 < \phi < 2\pi)$ integrals arise during the derivation of the RBC and are a consequence of the orthogonality relationships [18]. The half domain integrals $(0 < \phi < \pi)$ are due to the restriction of the finite element solution to the half domain, Γ_2 [16,23].

2.6. Material properties

The MW thawing process is examined for the material tylose. Thermal and dielectric data at 2450 MHz for both the solid and liquid phases of tylose are given in Table 1. We have neglected buoyancy effects and assumed a constant value of 1000 kg m^{-3} for the density of both the liquid and solid phases of tylose. The material properties in the mushy region are functions of the liquid volume fraction ϕ_l, which is in turn a function of the temperature T. The functional form of ϕ_l vs T for tylose is similar to that used by Zeng and Faghri [13];

$$\phi_\mathrm{l} = \begin{cases} 0 & T < T_\mathrm{i} \\ \dfrac{(T - T_\mathrm{i})^2}{(T_\mathrm{f} - T_\mathrm{i})(T_\mathrm{m} - T_\mathrm{i})} & T_\mathrm{i} \leqslant T \leqslant T_\mathrm{m} \\ 1 - \dfrac{(T - T_\mathrm{f})^2}{(T_\mathrm{f} - T_\mathrm{i})(T_\mathrm{f} - T_\mathrm{m})} & T_\mathrm{m} \leqslant T \leqslant T_\mathrm{f} \\ 1 & T > T_\mathrm{f}, \end{cases} \qquad (38)$$

where T_m is the temperature at which the latent heat release is a maximum and T_f is the final thawing temperature. The parameter values for T_i, T_m and T_f, in Eq. (38) are 265, 270, and 272.4 K respectively. Fig. 3a illustrates the ϕ_l vs T relationship for tylose and Fig. 3b depicts the dependence of wavelength of radiation in the medium λ_m and penetration depth D_p calculated using the dielectric properties obtained from Eq. (13). Since the frozen state of the sample has a lower dielectric loss both λ_m and D_p are higher for the frozen sample and decrease with an increase in liquid volume fraction. Note that the particular functional form of Eq. (38) yields a continuous $C_\mathrm{eff}(T)$ function [10].

Table 1
The thermal and dielectric properties are given for tylose in the solid (s) and the liquid (l) phases [4]

Material property	Tylose (s)	Tylose (l)
Heat capacity, C_p (W s kg^{-1} °C^{-1})	2090	3520
Thermal conductivity, k (W m^{-1} °C^{-1})	1.3	0.5
Density, ρ (kg m^{-3})	961	1057
Latent heat, λ (J kg^{-1})	2.34×10^5	
Dielectric constant (2450 MHz), κ'	6.0	50.0
Dielectric loss (2450 MHz), κ''	1.5	17.0

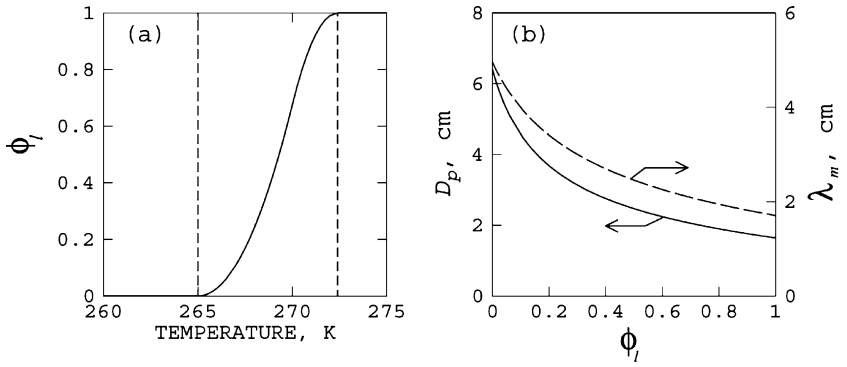

Fig. 3. Variation of (a) liquid volume fraction, ϕ_l (Eq. (38)) with temperature and (b) Penetration depth, D_p and wavelength of radiation in the medium, λ_m (Eqs. (10) and (11)) with ϕ_l for tylose. Note that both D_p and λ_m decrease with increasing liquid volume fraction.

2.7. Numerical tests

We first tested the implementation of the radiation boundary condition for the half domain by comparing the MW power computed with the full domain radiation boundary condition. In all the cases we found that the comparisons were excellent. Fig. 4 is a representative comparison. In addition we tested our computational method, in the absence of MWs for heat conduction with Dirichlet boundary conditions and compared our results for heat conduction in the presence of MWs with an earlier work by Ayappa et al. [18].

MW thawing simulations are carried out for cylinders of radii varying from 0.5 to 5 cm. The heat transfer coefficient, h, was chosen to be 2 $W m^{-2} K^{-1}$. Unless otherwise stated the sample is initially kept at the initial melting point of 265 K, for tylose. Typically a small time step $\Delta t = 1 \times 10^{-4}$ s was used at the first time step and a $\Delta t = 0.03$ s was used for subsequent steps. Based on spatial and temporal refinements a 64 element grid and time step of 0.03 s was used in the computations. All λ_m and D_p values reported are based on spatially averaged dielectric properties. The average power and temperature profiles were obtained by integrating across the sample cross section.

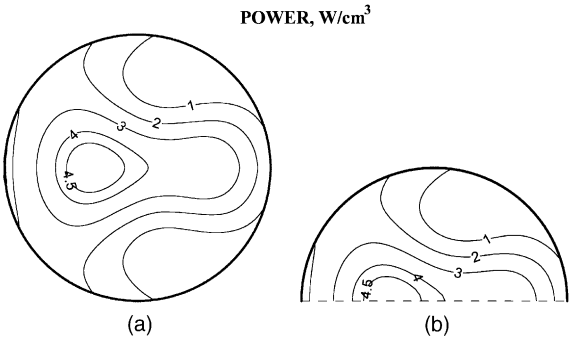

Fig. 4. Power profiles for (a) based on circular domain and (b) half domain. The dielectric and thermal properties are similar to those used by Ayappa et al. [18]. $f = 2800$ MHz, $I_0 = 3$ $W cm^{-2}$, $\kappa' = 42.6$ and $\kappa'' = 13.1$.

3. Results

Figs. 5–9 illustrate the spatial distribution of absorbed MW power, temperature and liquid volume fractions at different times during thawing for cylinder diameters ranging from $D = 0.2$ to 10 cm. In all cases the cylinders were exposed to MWs of intensity 1 $W cm^{-2}$ from the left face and the computations were stopped when the entire sample was thawed, i.e. the liquid volume fraction $\phi_l = 1$ for the entire cylinder. Unless stated otherwise, the shaded regions in the figures represent the fully thawed liquid regions. Since the initial temperature of the sample is at the initial melting point ($T = 265$ K) for tylose, the entire sample turns mushy during the early stages of thawing. An example of thawing in a sample whose initial temperature (255 K) is below the initial melting point is illustrated later.

For the $D = 0.2$ cm sample (Fig. 5) the penetration depth D_p is much larger than the sample diameter, resulting in uniform power absorption. As a consequence the temperature and liquid volume fractions show little variation in the sample during thawing, and the liquid forms almost simultaneously throughout the sample at 1.27 min. At $D = 1$ cm (Fig. 6) the peak in the power at the unexposed face changes the dynamics during thawing. Thawing is initiated from the unexposed face of the cylinder and propagates towards the exposed face with time. An interesting feature to note is the decrease in absorbed power at the incident face during thawing, resulting in a smaller increase in temperature at the incident face when compared with the temperature rise at the unexposed face.

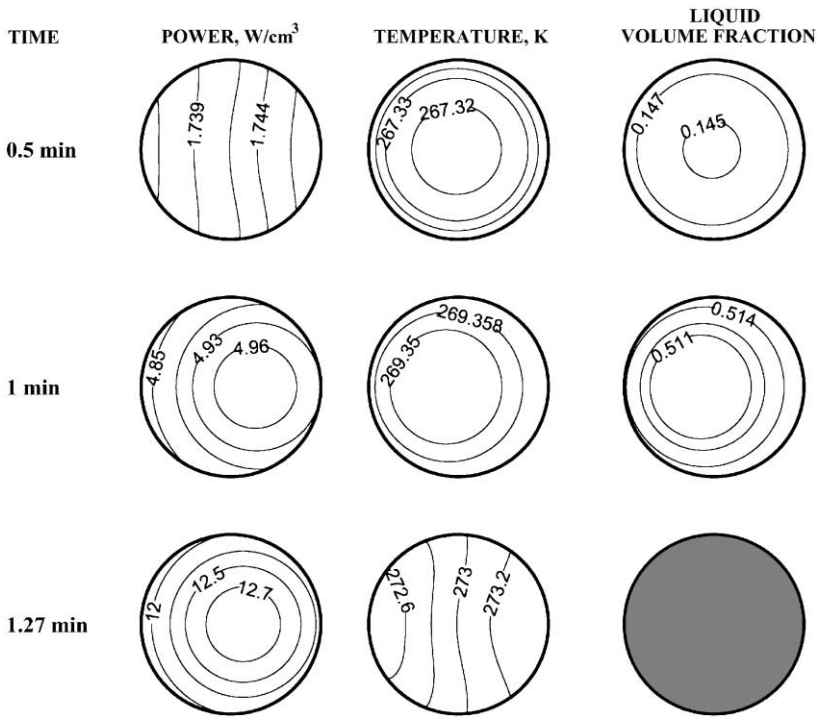

Fig. 5. Power, temperature, and liquid volume fraction contours, during MW thawing of a $D = 0.2$ cm cylinder exposed to MWs from the left (exposed) face. Uniform power absorption results in simultaneous formation of liquid across the sample.

In contrast to the $D = 1$ cm sample, at $D = 2$ cm (Fig. 7) although thawing originates from the face not exposed to MWs, enhancement in the power being absorbed at the incident face gives rise to two liquid regions which move towards each other. These multiple liquid regions which frequently arise due to the penetration of MWs are captured without resorting to remeshing in the effective heat capacity method. As the cylinder diameter is increased to $D = 4$ cm (Fig. 8) thawing is no longer initiated at the outer unexposed face but at the center of the cylinder. At intermediate stages the liquid region extends from the unexposed face toward the sample center, and in contrast to the previous case, the liquid front moves from left to right. The situation where the sample diameter is larger than the maximum penetration depth of $D_p = 6.4$ cm (based on the solid state dielectric properties) is illustrated in Fig. 9. Here in contrast to the smaller samples, power is mainly deposited at the incident face and thawing proceeds with the formation of a single liquid region which grows toward the regions of low power absorption.

As mentioned earlier, Figs. 5–9 illustrate cases where the initial temperature of the sample was kept at the initial melting point. Fig. 10 is a representative simulation for a $D = 10$ cm sample where the initial temperature is 255 K, 10° below the initial melting point of 265 K. The figure illustrates an intermediate situation where the sample consists of coexisting mush and solid regions. Even for this large sample diameter the entire region turns mushy prior to the appearance of liquid regions.

Fig. 11 illustrates the average power and temperature distributions for samples with diameters 0.2, 1, 4 and 10 cms. The forms of the average power are illustrative of the trends we have observed. At $D = 0.2$ cm the power increases monotonically, and the opposite occurs at $D = 10$ cm where the power decreases monotonically. At intermediate sample diameters, the power shows one or two maxima indicative of a resonant situation. The average temperatures shown in Fig. 11 indicate that the heating rates are high during the initial stages of thawing and increase during a resonance. For the larger samples the average temperature rise is linear, indicative of a constant heating rate. The total thawing times for the various cylinders plotted in Fig. 12 show a monotonic increase in thawing time. However due to resonances that occur in the smaller cylinders we were unable to fit the data to a power law, as indicated in the log–log plot shown in the inset of Fig. 12.

4. Discussion

In order to explain the thawing trends presented above and arrive at guidelines for predicting the possible

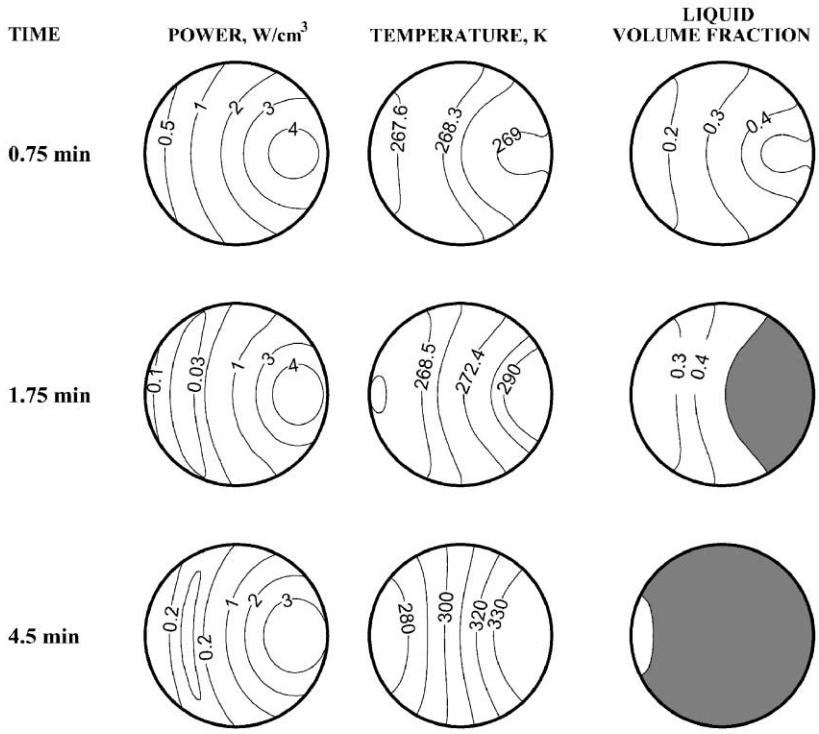

Fig. 6. Similar to Fig. 5 with $D = 1$ cm. Due to increased power absorption, liquid regions form first at the unexposed face and the thawing front moves from the unexposed face to exposed face. This cylinder diameter corresponds to a maximum in the average power for pure solid (Fig. 13) and a minimum in the power for pure liquid (Fig. 13).

scenarios, it is instructive to understand the power distributions for the pure solid and pure liquid states, which serve as the two extreme states for the system. Figs. 13 and 14 illustrate the average power as a function of cylinder diameter for the pure solid and liquid states respectively. Insets in the figure illustrate the distribution of power within the sample indicating the D/D_p and D/λ_m ratios. $D_p = 6.4$ cm and $\lambda_m = 4.956$ cm for the solid state and $D_p = 1.64$ cm and $\lambda_m = 1.706$ cm for the liquid state. These two length scales determine the pattern of power absorption in the sample. Maxima and minima in the average power plots vs cylinder diameter illustrate the phenomenon of resonances during MW power absorption [17]. At a resonance the power absorption is maximum due to constructive interference within the sample. However as the cylinder diameter is varied, destructive interference can lower the power absorbed resulting in a minimum. The resonances also get weaker as the sample diameter is increased.

For the $D = 0.2$ cm sample, D/D_p and D/λ_m are much smaller than unity for both the solid and liquid (thawed) states. Hence the absorbed power shows little spatial variation during the entire transformation from solid to liquid, resulting in uniformity in both the temperatures and liquid volume fraction across the cylinder (Fig. 5). The plot of the average power Fig. 11a illustrates a monotonic increase during thawing which is consistent with the increase in the average power absorption from the solid to liquid states (due to the higher liquid state dielectric loss; see Table 1) as seen by comparing Fig. 13 with Fig. 14 at $D = 0.2$ cm.

As the diameter increases to 1 cm the maximum in the power shifts toward the unexposed face for both the frozen and liquid states (Fig. 6). Here the D/D_p is still small and the D/λ_m ratio varies from about 0.2 in the solid to about 0.6 in the liquid. At these length scales, the sample lies in the regime of unexposed side power absorption as seen in Figs. 13 and 14, and liquid regions move from the unexposed side toward the exposed face. Another interesting feature to note here is that in the solid state the 1 cm diameter corresponds to a resonant point in the average power (Fig. 13). However this diameter also corresponds to a minimum in the average power when fully thawed (Fig. 14). As indicated earlier, this movement away from a resonant point during thawing leads to a decrease in the absorbed power at the incident face (Fig. 6). Since the power absorption in the liquid is still higher than that of the solid, there is a slight increase in the average power from the solid to liquid states as seen in Figs. 13 and 14.

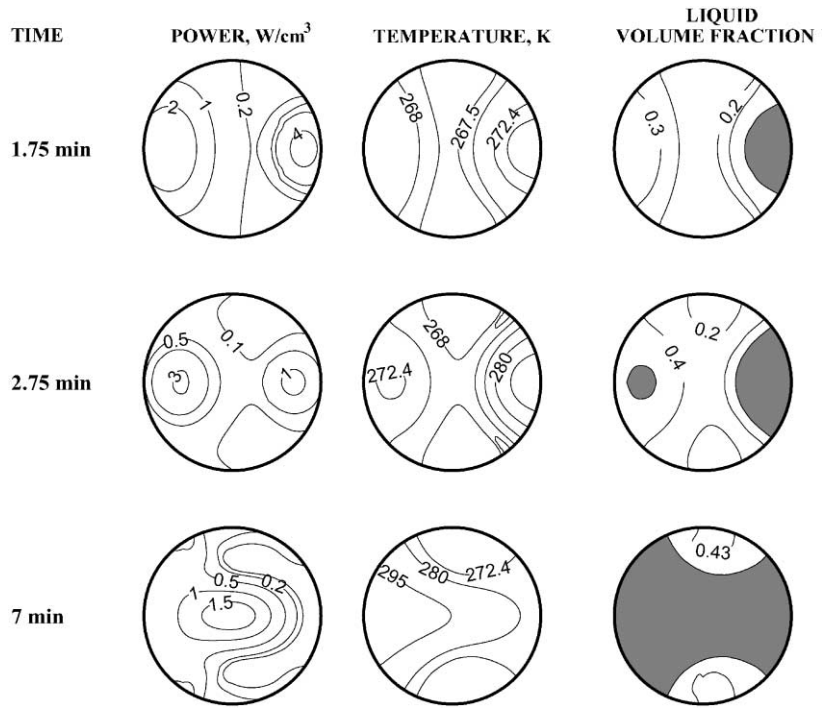

Fig. 7. Similar to Fig. 5 with $D = 2$ cm. Here although thawing is initiated at the unexposed face, melting also occurs near the exposed face and two liquid regions are formed during intermediate stages of thawing.

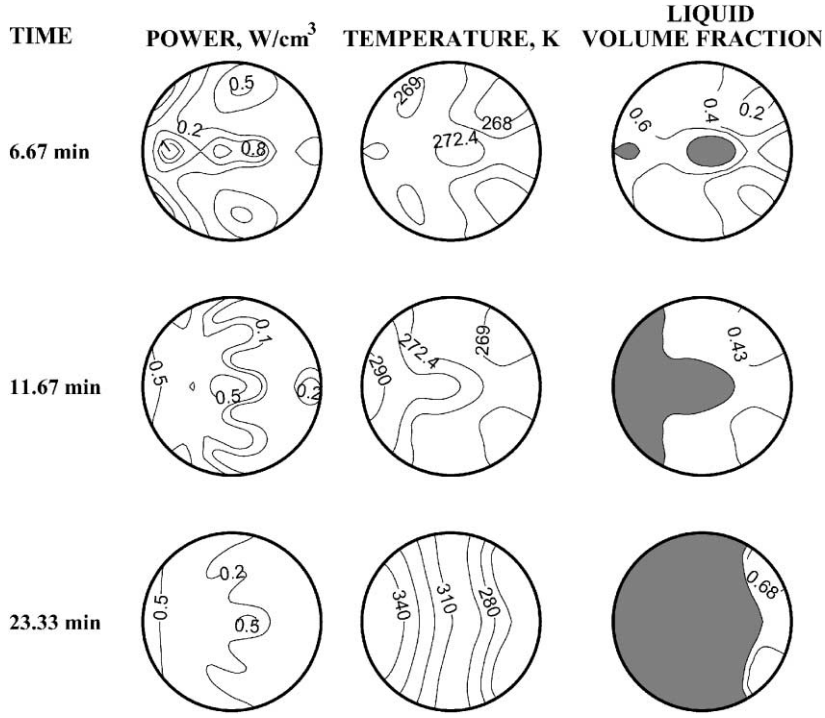

Fig. 8. Similar to Fig. 5 with $D = 4$ cm. Thawing proceeds primarily from the central and exposed faces of the sample.

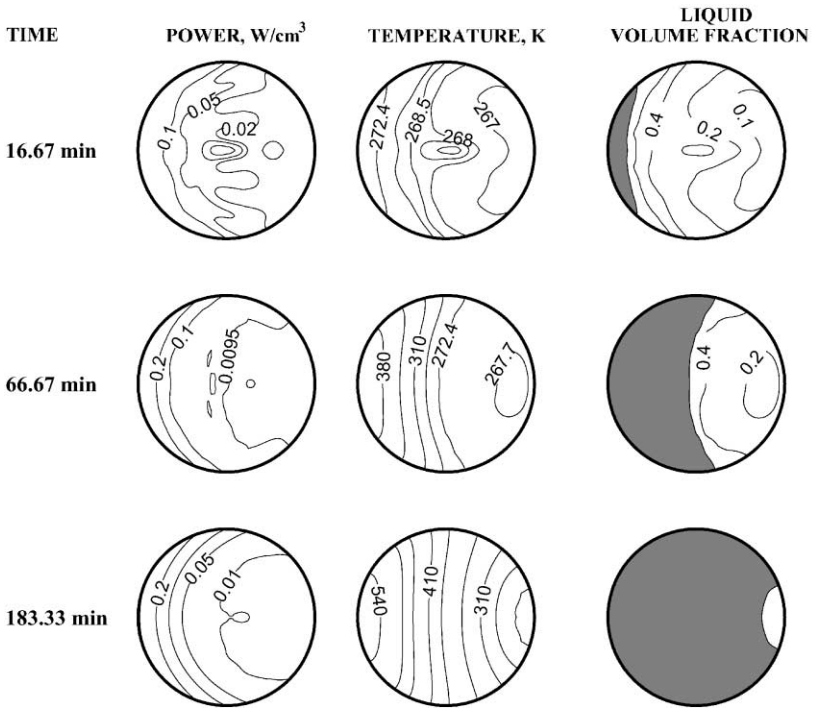

Fig. 9. Similar to Fig. 5 with $D = 10$ cm. At this large sample diameter both D/D_p and $D/\lambda_m \gg 1$ and thawing proceeds from the exposed face. Due the large D/D_p ratio the power decays from the exposed face of the sample, following a Lambert's law behavior.

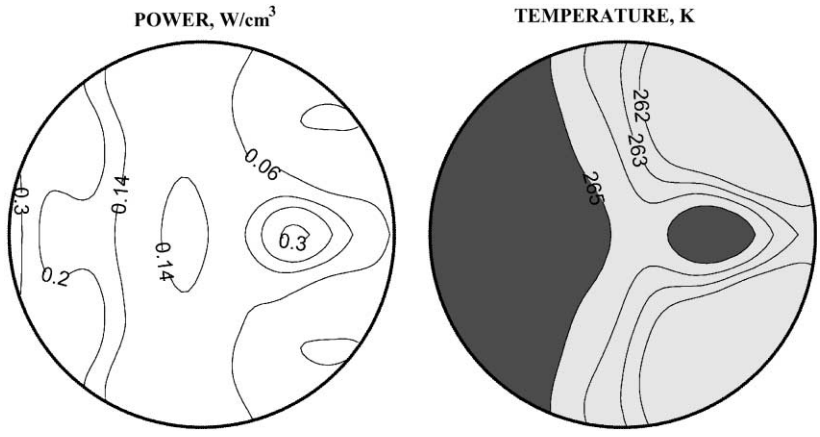

Fig. 10. Similar to Fig. 5 with $D = 10$ cm and a initial temperature of 255 K. In this case, unlike the previous cases where the initial temperature of the sample is at the melting point, no liquid regions are formed and the sample consists of solid (light shade) and mushy (darker shade) regions.

For the 2 cm sample D/D_p varies from 0.3 to 1.2 from solid to liquid and D/λ_m from 0.4 to 1.1. This is an intermediate situation and at these D/λ_m ratios although, the power absorption starts out at the unexposed side, the increase in D/λ_m ratio shifts the situation to one where power is deposited at the exposed face as well. This situation can be observed in the Figs. 13 and 14 where the power shifts from the unexposed side to both faces as D/λ_m ratio increases. Further the power absorption in intermediate states is qualitatively similar to situations with the same D/λ_m ratios. This can be seen on examining the intermediate states for the $D = 2$ cm sample (Fig. 7) with the liquid state power distributions shown at intermediate D/λ_m ratios in Fig. 14, indicating

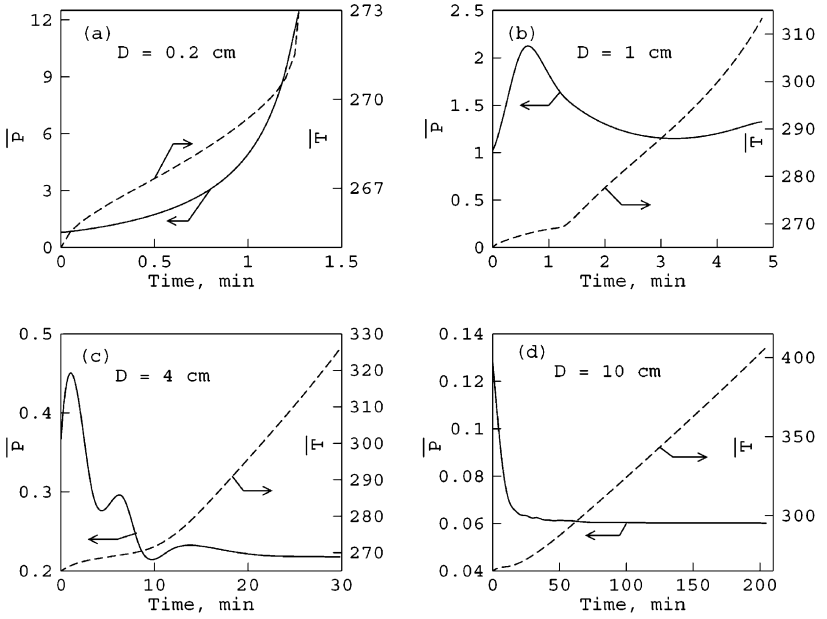

Fig. 11. Average power and temperature for cylinders during MW thawing. For Regime I, thawing (a) the power increases monotonically during thawing. For Regime II thawing (b) and (c), resonances occur during intermediate stages of thawing which lead to local maxima in the average power. For Regime III samples (d) the average power decreases monotonically.

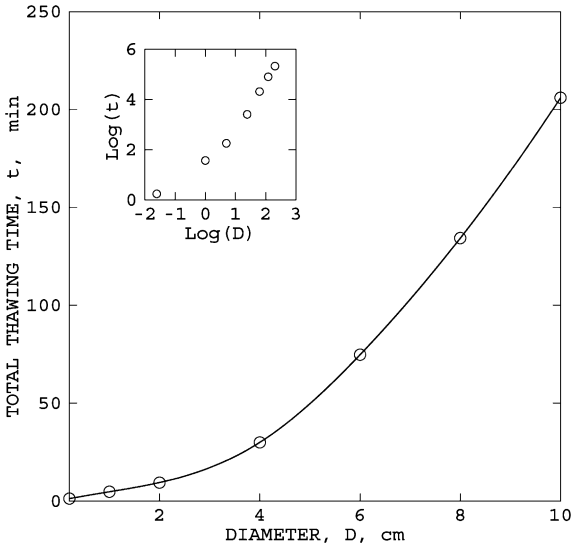

Fig. 12. Total thawing time (t) vs sample diameter (D) is shown during MW thawing. The inset shows a log–log plot indicating the absence of a power law trend attributed to resonant conditions at intermediate diameters.

the power absorption patterns in the pure liquid control thawing for the most part. At $D = 4$ cm, although power absorption in the pure solid occurs at both the exposed and unexposed face, the absorption shifts to center and exposed face heating as seen in the pure liquid power absorption (Fig. 14). This is reflected in Fig. 8, where the liquid region extends from the exposed face to the center during the 11th min.

For the largest diameter studied, $D = 10$ cm and $D/D_p = 6.1$ for the liquid and $D/\lambda_m = 5.8$. At these large D/D_p ratios power absorption is exponentially decaying (Lambert's law regime) from the exposed face. Although there is some power absorption at the unexposed face at the initial stages (Fig. 14) the rapidly increasing D/D_p ratio dominates the dynamics and melting is seen to occur from the exposed face. The plot of the average power during thawing (Fig. 11c) is a monotonically decreasing function. Although the frozen sample has a lower dielectric loss, the low D/D_p ratio permits power absorption through the sample. In contrast power is absorbed only in a small region at the unexposed end for the liquid. This decrease in power for the $D = 10$ cm sample for the liquid state is also seen in Fig. 14.

From our discussion above we find the manner in which the liquid regions form within the sample is a strong function of the D/D_p and D/λ_m ratios of the fully thawed or liquid state. In an effort to generalize the possible scenarios that might occur during thawing of cylindrical samples we make a qualitative phase plot of D/D_p vs D/λ_m as shown in Fig. 15. For samples with small D/D_p and D/λ_m ratios (Regime I) power absorption shows little variation and thawing occurs more or less uniformly throughout the sample. For intermediate

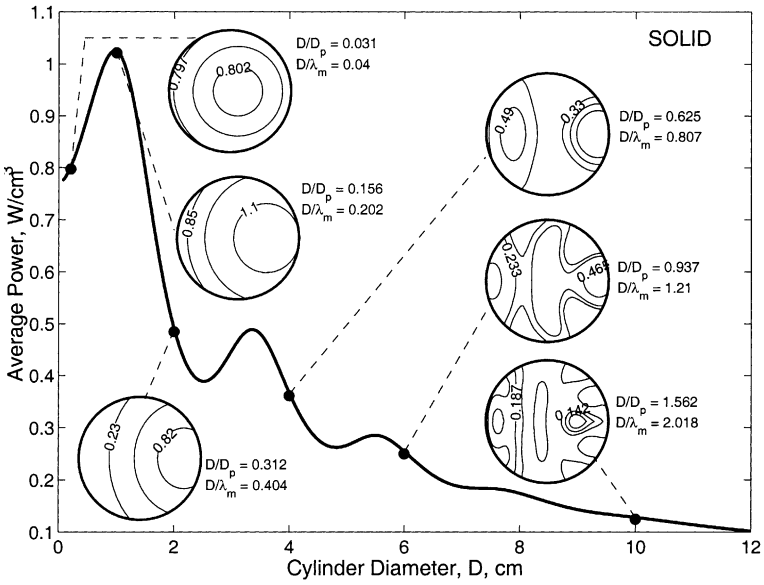

Fig. 13. Average power for the pure solid sample as a function of cylinder diameter. The inset show the spatial variation in power for cylinder diameters whose thawing dynamics have been computed. D/D_p and D/λ_m values are also shown.

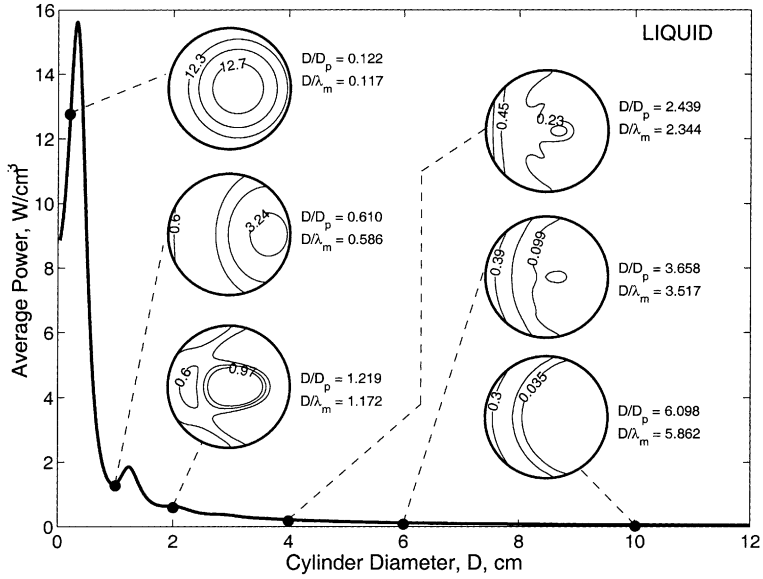

Fig. 14. Average power for the pure liquid sample as a function of cylinder diameter. The inset show the spatial variation in power for cylinder diameters whose thawing dynamics have been computed. D/D_p and D/λ_m values are also shown.

values of D/λ_m and D/D_p (Regime II) thawing can occur from the unexposed face, both unexposed and exposed faces and from the central and exposed regions as D/λ_m increases within Regime II. Since D/D_p and D/λ_m are approximately order one in Regime II, it is here that the power distribution shows the largest variation from solid to liquid state. For large D/D_p ratios (Fig. 9, $D = 10$ cm) the MW power is a maximum at the exposed face from where thawing is initiated. This is the Lambert law regime for the MW power. In the transition from Regime I to II thawing originates from the unexposed face (Fig. 7, $D = 2$ cm) and in the transition region from

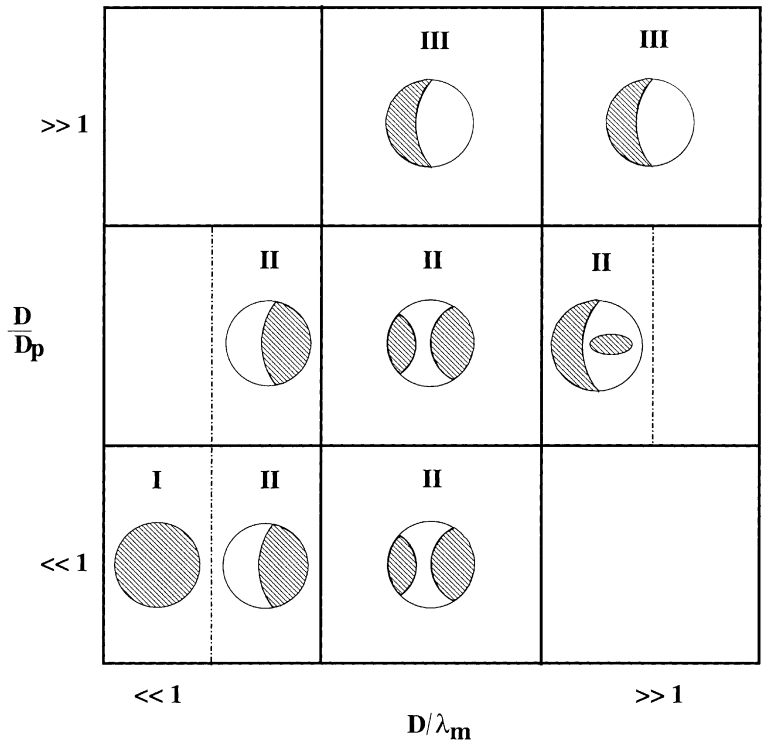

Fig. 15. Schematic diagram of D/D_p vs D/λ_m summarizing the various regimes that have been observed, based on the formation of liquid regions within the sample.

Regime II and III thawing occurs both from the central and exposed regimes of the sample (Fig. 8, $D = 4$ cm) as illustrated in Fig. 15. The blank regions in Fig. 15 are not representative of the typical D/D_p and D/λ_m ratios observed for most biological materials. In general the temperature variations within the sample are the least in Regime I and are the largest in Regime III.

Before concluding we digress briefly to discuss the resonances during intermediate stages of thawing that give to a maxima in the average power (Fig. 11) for cylinders that lie in Regime II. Resonances in cylindrical samples have been extensively investigated by Ayappa et al. [17] where the cylinder diameters at which resonances occur were predicted using by $D/\lambda_m = 0.5n - 0.257$ where $n = 1, 2, \ldots$ ($n = 1$ corresponds to the first resonance peak and so on) (Table 2). The above relation was derived for materials whose dielectric properties and hence wavelength of radiation in the medium are constant throughout the sample. However, in the present study where the wavelength is a function of the position in the sample the standing wave patterns are more complex and resonances may at best be related to an average wavelength in the medium. Using the spatially averaged value of λ_m at a resonant point from our simulations for a given sample diameter D, we obtained the closest value of n from the relationship given above.

Table 2
A comparison of λ_m (cm) between the correlation of Ayappa et al. [17] and the present case based on spatial averaged ($\bar{\lambda}_m$) values during thawing

Diameter, D (cm)	λ_m (cm) (Ayappa et al., [17])	n	$\bar{\lambda}_m$ (cm) during thawing
1	4.115	1	3.108
2	2.69	2	2.74
4	3.218	3	3.879
	2.294	4	2.357

Using this n we obtained the value of λ_m at which the resonance would occur if the material had constant dielectric properties. The greatest discrepancy between the λ_m values occurs at $D = 1$ cm. Although there is a discrepancy at $D = 1$ cm, for the other sample diameters the results based on spatially averaged dielectric properties are in moderate agreement. Since the dielectric properties are spatially dependent estimates for the resonant conditions based on an average wavelength may not be completely reliable. The absence of resonant conditions for Regime I and III can be deduced from the average power plots Figs. 14 and 13 where both these regimes lie below and above the resonant regions respectively.

5. Conclusion

We have carried out extensive computations to investigate the thawing dynamics for frozen cylinders of tylose. Using the Galerkin finite element method the electric field equations are solved along with the effective heat capacity formulation of the energy balance equation. The effective heat capacity method, which is based on a fixed grid, is able to capture the multiply connected liquid regions that form due to the penetration of MWs.

Our computations illustrate that the thawing of cylinders can be classified into three distinct regimes based on the D/D_p and D/λ_m ratios of the fully thawed state. In Regime I where D/D_p and D/λ_m are much less than unity, thawing occurs more or less uniformly throughout the sample. For increasing values of D/D_p and D/λ_m (Regime II) the thawing originates from the unexposed face of the sample which is a transition regime and moves into a situation where thawing occurs from both faces or from the central and exposed faces with increase in D/λ_m. Finally for large D/D_p ratios (Regime III) thawing occurs from the exposed face due to the low penetration depth in the sample. The average power absorbed by the sample shows a monotonic increase in Regime I and a monotonic decrease in Regime II. In Regime II the power shows one or more local maxima due to a resonant condition. Temperatures show the least variation in Regime I and the greatest in Regime III. Usually power cycling is used in domestic and industrial ovens to control the temperature during MW thawing. We have illustrated this procedure of power cycling in our previous thawing study in 1D [10].

The effective heat capacity method used in this study is appropriate for materials which melt over a temperature range. The formulation avoids complex front tracking algorithms, and simplifies the solution for the electric field since the dielectric properties also vary continuously from solid to liquid. For the formulation to be valid, the continuous variation of the properties across phase boundaries is a necessary condition. This will always be true if the solid and liquid regions are separated by a mushy region. This condition has not been violated in all the melting situations investigated in our study. However, while studying melting in a pure material scattering at the solid–liquid interface must be incorporated with appropriate interface conditions if the traditional front tracking methods are used. Nevertheless this can be circumvented by using the enthalpy formulation by incorporating a pseudo-mushy region [16].

Our study has laid emphasis on understanding the thawing dynamics and its relation to two length scales, D/D_p and D/λ_m within the sample. Notwithstanding the restriction of our study to a specific material (tylose), the conclusions based on the length scales are expected to be general. The exact temporal behavior will naturally depend on the specific material involved. We also conclude that the power distribution in the final liquid (thawed) state is a dominating factor in predicting the formation of liquid regions. Although our study has been carried out for an idealized 2D configuration, a similar approach can be used to develop predictive models for an industrial process. In perspective, our model based on the effective heat capacity formulation indicates the efficacy in handling multiple thawing fronts that are common to a MW based thawing process.

References

[1] R.E. Mudgett, Microwave food processing, Food Technol. 43 (1989) 117–126.
[2] U. Rosenberg, W. Bogl, Microwave thawing, drying and baking in the food industry, Food Technol. 41 (1987) 85–91.
[3] H.S. Carslaw, J.C. Jaeger, Conduction of Heat in Solids, Clarendon Press, Oxford, 1959.
[4] P. Taoukis, E.A. Davis, H.T. Davis, J. Gordon, Y. Talmon, Mathematical modeling of microwave thawing by the modified isotherm migration method, J. Food Sci. 52 (1987) 455–463.
[5] B.P. Pangrle, K.G. Ayappa, H.T. Davis, E.A. Davis, J. Gordon, Microwave thawing of cylinders, Am. Inst. Chem. Eng. J. 37 (1991) 1789–1800.
[6] B.P. Pangrle, K.G. Ayappa, E. Sutanto, H.T. Davis, E.A. Davis, J. Gordon, Microwave thawing of lossy dielectric materials, Chem. Eng. Commun. 112 (1992) 39–53.
[7] A.J. Dalhuijsen, A. Segal, Comparison of finite element techniques for solidification problems, Int. J. Numer. Meth. Eng. 23 (1986) 1807–1829.
[8] J.A. Dantzig, Modelling liquid–solid phase changes with melt convection, Int. J. Numer. Meth. Eng. 28 (1989) 1769–1785.
[9] V.R. Voller, C.R. Swaminathan, B.G. Thomas, Fixed grid techniques for phase change problems: A review, Int. J. Numer. Meth. Eng. 30 (1990) 875–898.
[10] T. Basak, K.G. Ayappa, Analysis of microwave thawing of slabs with effective heat capacity method, Am. Inst. Chem. Eng. J. 43 (1997a) 1662–1674.
[11] M. Bhattacharya, T. Basak, K.G. Ayappa, A fixed-grid finite element based enthalpy formulation for generalized phase change problems: role of superficial mushy region, Int. J. Heat Mass Transfer, PII: S0017-9310(02)00178-3.
[12] C.J. Coleman, The microwave heating of frozen substances, Appl. Math. Model. 14 (1990) 439–443.
[13] X. Zeng, A. Faghri, Experimental and numerical study of microwave thawing heat transfer for food materials, ASME—J. Heat Transfer 116 (1994) 446–455.
[14] K.G. Ayappa, Modelling transport processes during microwave heating: A review, Rev. Chem. Eng. 13 (1997a) 1–69.
[15] T. Basak, K.G. Ayappa, Analysis of microwave thawing with the effective heat capacity method, in: Proceedings of the Third ISHMT-ASME Heat and Mass Transfer Conference, and Fourteenth National Heat and Mass Transfer Conference, 1997b, pp. 289–293.

[16] T. Basak, K.G. Ayappa, Influence of internal convection during microwave thawing of cylinders, Am. Inst. Chem. Eng. J. 47 (2001) 835–850.
[17] K.G. Ayappa, H.T. Davis, S.A. Barringer, E.A. Davis, Resonant microwave power absorption in slabs and cylinders, Am. Inst. Chem. Eng. J. 43 (1997b) 615–624.
[18] K.G. Ayappa, H.T. Davis, E.A. Davis, J. Gordon, Two-dimensional finite element analysis of microwave heating, Am. Inst. Chem. Eng. J. 38 (1992) 1577–1592.
[19] K.G. Ayappa, H.T. Davis, E.A. Davis, J. Gordon, Analysis of microwave heating of materials with temperature-dependent properties, Am. Inst. Chem. Eng. J. 37 (1991) 313–322.
[20] H. Fricke, The complex conductivity of a suspension of stratified particles of spherical or cylindrical form, J. Phys. Chem. 56 (1955) 168–174.
[21] M. Abramowitz, I.A. Stegun, Handbook of Mathematical Functions, ninth ed., Dover, New York, 1970.
[22] J.N. Reddy, An Introduction to the Finite Element Method, McGraw-Hill, New York, 1993.
[23] T. Basak, Analysis of microwave thawing, Ph.D. Thesis, Indian Institute of Science, Bangalore, India, 1999.